Applied Catalysis B: Environmental 328 (2023) 122505

Contents lists available at ScienceDirect

Applied Catalysis B: Environmental

journal homepage: www.elsevier.com/locate/apcatb

Elucidating reaction pathways occurring in CO_2 hydrogenation over Fe-based catalysts

Aleksandr Fedorov *, Henrik Lund, Vita A. Kondratenko, Evgenii V. Kondratenko, David Linke *

Leibniz-Institut für Katalyse e.V., Albert-Einstein-Str. 29a, 18059 Rostock, Germany

ARTICLE INFO

Keywords:
CO_2 hydrogenation
Segmental rates
Reaction pathways
Anderson-Schulz-Flory distribution

ABSTRACT

A detailed experimental analysis of reaction pathways proceeding in CO_2 hydrogenation over Fe-based catalysts was performed. The catalytic activity was measured at different degrees of conversion and used to analyze the production/consumption rates of reagents and products along the catalyst bed. It was demonstrated that except for the reverse water gas shift reaction and the subsequent hydrogenation of CO via Fischer-Tropsch (FT) mechanism, additional routes of hydrocarbon formation from CO_2 exist in the CO_2 hydrogenation. One of them is the methanation reaction which takes place over all studied catalysts. Another one is a direct pathway of C_{2+} hydrocarbon formation from CO_2 that plays a significant role at least for some catalysts. In this route, iron carbides may be responsible for hydrogenating CO_2 into C_{2+} hydrocarbons. Based on these results, the concept of requiring iron oxides as an essential active component for catalyzing the RWGS reaction in CO_2-FT should be reviewed.

1. Introduction

The increase in energy production and commodity products results in dramatic rise in emissions of carbon dioxide in the atmosphere. CO_2 is well-known to be the main reason of greenhouse effect, and thus, it motivates to develop new approaches and methods for reducing and controlling its emissions [1]. The capture of carbon dioxide and its chemical transformation to valuable organic compounds are considered as a perspective strategy for the development of clean and sustainable energy technologies [2–4]. They can be based on direct catalytic CO_2 hydrogenation with H_2 to higher hydrocarbons (CO_2-Fischer-Tropsch (CO_2-FT)) that is the one of a potential solution for the CO_2 emission problem [4–6].

It is generally accepted [7,8] that CO_2-FT synthesis proceeds through two stages: the endothermic reverse water gas shift reaction (RWGS, $CO_2 + H_2 \rightleftarrows CO + H_2O$) followed by the exothermic CO hydrogenation according to classical FT reaction (CO-FT, $CO + 2\ H_2 \rightarrow -(CH_2)- + H_2O$). The RWGS reaction has a thermodynamic limitation. The FT reaction has a kinetic limitation, wherein the fraction of hydrocarbons can be described by the Anderson-Schulz-Flory (ASF) distribution [9–11]:

$$W_n = n\cdot(1-\alpha)^2\cdot\alpha^{n-1}, \quad (1)$$

where n – carbon number; W_n – mass fraction of hydrocarbon with carbon number n; α – the chain growth probability that is defined as a ratio between the rate of the chain prolongation per the sum of the chain prolongation and termination rates [12,13].

Iron-based catalysts are usually applied for CO_2-FT, because they can catalyze both reactions [14–16]. It is considered that the RWGS reaction occurs on Fe_3O_4, while iron carbides (Fe_5C_2, Fe_3C etc.) formed in situ under reaction conditions are responsible for the CO-FT reaction [7]. Unpromoted Fe-based catalysts produce a lot of methane. To suppress this undesired reaction and to improve the performance of Fe-based catalysts to C_{2+} hydrocarbon production, various promoters are typically applied during catalyst preparation [17–24]. The most effective promoters are alkali metals (K, Na). They decrease CH_4 formation and increase the rate of CO_2 consumption and of C_{2+} hydrocarbon production. This positive effect is explained by an enhanced bonding strength of adsorbed CO_2 leading to a decrease in catalyst hydrogenation ability [18,25,26]. Moreover, alkali metals are able to accelerate the formation of Fe_5C_2 [27,28].

Kinetic modeling of CO_2 hydrogenation over Fe-containing catalysts is usually based on empirical Langmuir-Hinshelwood-Hougen-Watson (LHHW) models [14,29–31]. However, recently Carlotta Panzone et al. [32] proposed a detailed microkinetic model for CO_2 hydrogenation over a Fe-K/Al_2O_3 catalyst. All these models have been developed according to a two-stages mechanism of CO_2-FT, where the RWGS and

* Corresponding authors.
E-mail addresses: aleksandr.fedorov@catalysis.de (A. Fedorov), david.linke@catalysis.de (D. Linke).

https://doi.org/10.1016/j.apcatb.2023.122505
Received 19 December 2022; Received in revised form 13 February 2023; Accepted 20 February 2023
Available online 24 February 2023
0926-3373/© 2023 Elsevier B.V. All rights reserved.

FT reactions proceed over different active sites. The direct pathway of CO_2 hydrogenation to hydrocarbons via FT reaction was to our knowledge only considered in the paper published by Riedel et al. [14]. However, an experimental proof of the presence of direct route was not given. Besides, the data analysis of CO_2 hydrogenation catalysts performed by our group indicates the presence of the direct pathway for some catalytic systems [33]. Moreover, an additional pathway of direct CO_2 hydrogenation to methane, also known as the Sabatier reaction, was suggested and discussed in the works [15,34,35]. However, the reaction was not taken into account in kinetic modeling. Recently, Skrypnik et al. [3] performed the analysis of the spatial profiles of C_{2+} formation rates and composition distribution along the catalyst bed for CO_2-FT. It was demonstrated that the highest formation rate of C_{2+} hydrocarbons was observed at the front part of the bed, wherein, Fe was present in the form of Fe_5C_2 at this part of bed but not as iron oxide which is supposed to catalyze the RWGS reaction. From this we concluded that the two-stage mechanism may be a too simple model and Fe_5C_2 could possibly also catalyze the RWGS reaction. It should be also noted that the analysis of pathways was usually performed for CO, CH_4, and C_{2+} hydrocarbons; the individual analysis of the formation of each hydrocarbon has not been considered. Wherein, the ASF analysis of rates of hydrocarbon formation and especially the deviation from ASF distribution can give additional information about the mechanism of CO_2 hydrogenation.

Reviewing the literature on the CO_2-FT synthesis revealed that different pathways of CO_2 hydrogenation were suggested and considered. Despite a number of studies, there are still fundamental questions open regarding the mechanism and reaction pathways occurring in CO_2 hydrogenation into hydrocarbons. Thus, the present work is devoted to investigating and analyzing reaction pathways proceeding in the process of CO_2 hydrogenation to hydrocarbons using typical Fe-based catalysts. For this, the iron-based catalysts with/without different dopants (K, K and Mn, K and Al) were synthesized by using an organic-combustion method that is effective for the preparation of highly active and selective catalysts in direct CO_2 hydrogenation to hydrocarbons [7]. K was chosen as dopant because it is the most effective and preferable promoter for improving the performance of Fe-based catalysts [33,36–39]. Mn is the most effective transitional metal as a dopant for Fe-based catalysts according to statistical analysis [17,40]. Moreover, a synergic effect between Mn and K metals was reported in work [41]. Al dopant was chosen as a textural promoter [14]. The obtained catalysts were tested in CO_2 hydrogenation. By varying the residence time, we obtained data on product selectivity in a wide range of CO_2 conversion from 2.5 % to 30 % in small increments of CO_2 conversion which allowed estimating rates of reagents consumption and products formation along the catalyst bed using simple arithmetic operations and analyze the mechanism of CO_2 hydrogenation without kinetic modeling. The ASF distribution was used for analyzing the rates of hydrocarbon formation.

2. Experimental part

2.1. Catalyst synthesis

In this study, the catalysts were obtained by an organic-combustion method. The solutions of nitrates and citric acid (CA) were prepared by mixing iron (III) nitrate nonahydrate (99.0 %, Merck), potassium nitrate (99.7 %, Fischer Chemical), aluminum nitrate nonahydrate (98 %, ChemPure), manganese (II) nitrate hydrate (97 %, Sigma Aldrich), and citric acid monohydrate (99.5 %, ChemSolute), in distilled water. The obtained solutions (the solution volume is around 100 cm^3 for the preparation of ~ 3.5 g of catalyst, the concentrations of compounds in the solutions are presented in the Table 1) were heated in air up to 200 °C (the heating rate was 1 K/min) in an electrically oven and hold at this temperature up to combustion of the mixtures.

The obtained deposits were removed from the oven and crushed in a mortar. Resulting powders were heated in air up to 600 °C (ramp 10 K/min) and finally calcined at 600 °C for 4 h in an electrically oven. The samples were marked as Fe, Fe-K, Fe-K-Al, and Fe-K-Mn. The molar ratio of Fe:K and Fe:(Al or Mn) was 10:1 in the promoted catalysts. Molar ratios of citric acid (CA) to precursor metal ion were CA:Fe = 5:6, CA:K = 5:18, CA:Al = 5:6, and CA:Mn = 1:2 which corresponds to the stoichiometric amount required for the combustion reaction between metal nitrate and citric acid. As an example, the reaction between iron nitrate and citric acid can be written as:

$$6Fe(NO_3)_3 \cdot 9H_2O + 5C_6H_8O_7 \cdot H_2O \rightarrow 3Fe_2O_3 + 9N_2 + 30CO_2 + 79H_2O \quad (2)$$

The mass ratio water:(citric acid + precursor) was 5.0.

Table 1
The concentrations of compounds in the solutions used for the catalyst preparation.

The sample	Concentration, M				
	$Fe(NO_3)_3$	KNO_3	$Al(NO_3)_3$	$Mn(NO_3)_2$	$C_6H_8O_7$
Fe	2.0	–	–	–	1.67
Fe-K	2.0	0.2	–	–	1.72
Fe-K-Al	2.0	0.2	0.2	–	1.89
Fe-K-Mn	2.0	0.2	–	0.2	1.82

2.2. Catalyst characterization

To determine the surface area of the catalysts, low-temperature nitrogen adsorption-desorption isotherms were obtained at − 196 °C using BELSORP-max II (BEL Japan, Inc.) instrument. Before the measurements, the samples were heated in vacuum at 250 °C for 2 h. The initial branch of N_2 adsorption isotherm in the range of P/P_0 (0.05–0.25) was used to calculate the BET surface area.

The mass fraction of Fe, K, Al, and Mn in the catalysts was determined by inductively coupled plasma optical emission spectroscopy (ICP-OES) on Varian 715-ES ICP-Emission-Spectrometer. 10 mg of each sample was mixed with 8 ml of aqua regia. The sample preparation system “Multiwave PRO” from Anton Paar was used at 220 °C and 50 bar for the sample digestion with a microwave-assisted method. The digested solution was filled up to 100 ml and measured with ICP-OES. The data analysis was performed on the Varian 715-ES software “ICP Expert”.

The tests of temperature-programmed reduction with hydrogen (TPR-H_2) were performed in an in-house build set-up equipped with 8 quartz tubular reactors connected to an on-line mass spectrometer (Pfeiffer OmniStar GSD 300 01) for analysing the outlet gas flow. Before the tests, the samples were placed inside the reactor and heated up to 300 °C in a flow of Ar (20 ml/min) for 4 h. After cooling down to room temperature, a flow (5 % H_2 in Ar) was fed (20 ml/min) to the reactors followed by heating up to 900 °C with a constant heating rate 10°/min. The atomic mass units 2 (H_2) and Ar (40) were used to determine the H_2 concentration.

XRD powder patterns were recorded on a Stoe Stadi P transmission diffractometer equipped with a DECTRIS Mythen2 1 K detector applying Ge (111) monochromatized Mo Kα1 radiation (50 kV, 40 mA, 0.70930 Å). The samples were ground to a fine powder and placed between two acetate foils before the measurement. Data acquisition was done with 0.01 s^{-1}. Peak positions and profiles were fitted with Pseudo-Voigt function using the HighScore Plus software package (Panalytical). Phase identification was done by using the PDF-2 database of the International Center of Diffraction Data (ICDD). To estimate content of Fe-containing phases in the samples, the reference intensity ratio (RIR) method [42] was used; n-paraffin and $MnCO_3$ phases were neglected when estimating the fraction of carbidic and oxidic iron phases in the obtained catalysts. It is worth noting that we tried to apply the Rietveld method for determination of phase composition but due to the complexity of phase composition of the studied samples we were not able to obtain reliable results.

2.3. Transient experiments and their kinetic evaluation

Mechanistic and kinetic aspects of CO_2 and H_2 adsorption over the catalysts tested in CO_2 hydrogenation (the spent catalysts) were studied in the temporal analysis of the product reactor (TAP-2) system, which was described in detail in Refs. [43–45]. In a typical experiment, each catalyst (14 mg, 250–350 μm fraction) was placed in a home-made quartz-tube reactor within its isothermal zone between two layers of quartz particles of the same size. Previous to pulse experiments, the catalyst was heated in H_2-CO_2 mixture (H_2 flow rate was 4.50 $cm^3 \cdot min^{-1}$; CO_2 flow rate was 1.94 $cm^3 \cdot min^{-1}$) from room temperature to 300 °C and held at this temperature for 2 h. After that the reactor was evacuated to ca. 10^{-5} Pa.

Transient experiments with CO_2/Ar = 1:1 or H_2/D_2/Ar = 1:1:1 mixtures were performed at 300 °C in the single pulse mode. The mixtures were prepared using H_2 (Air Liquide, 5.0), D_2 (CK Special Gases Limited, 2.8), CO_2 (Air Liquide, 4.5) and Ar (Air Liquide, 5.0) without additional purification. In experiments with CO_2 the pulse size was below 10^{15} molecules per pulse to ensure Knudsen diffusion regime. The composition of the gases leaving the reactor was quantitatively analyzed by a quadrupole mass spectrometer (HAL RC 301 Hiden Analytical). The following atomic mass units (AMUs) were used for mass-spectrometric identification of different compounds: 44 (CO_2), 32 (O_2), 28 (CO_2, CO), 4 (D_2), 3 (HD), (H_2) and 40 (Ar). Pulses were repeated 10 times for each AMU and averaged to improve the signal-to-noise ratio. The concentration of each gaseous component was calculated from the ratio of the area of signal recorded at the respective AMU to the area of Ar. The fragmentation patterns and sensitivity factors required for the calculations were determined separately by pulsing the same mixtures in the reactor filled only with quartz particles. Using a model-free approach developed for this technique, [46] the experimental responses of CO_2 and Ar were transformed into the dimensionless form according to Eqs. (3) and (4). Such transformation allows to unambiguously determine the type of interactions (diffusion, reversible, or irreversible adsorption) of feed components with catalysts.

$$Dimensionless\ flow = \frac{flux(CO_2\ or\ Ar)\cdot reactor\ length^2}{N(CO_2\ or\ Ar)\cdot D^{eff}_{Knudsen}(CO_2\ or\ Ar)} \tag{3}$$

$$Dimensionless\ time = \frac{t\cdot D^{eff}_{Knudsen}(CO_2\ or\ Ar)}{reactor\ length^2} \tag{4}$$

$$Flux(CO_2\ or\ Ar) = I(CO_2\ or\ Ar)\frac{N(CO_2\ or\ Ar)}{\int_0^t I(CO_2\ or\ Ar)dt} \tag{5}$$

where $I(CO_2\ or Ar)$, $N(CO_2\ or\ Ar)$, and $D^{eff}_{Knudsen}(CO_2\ or\ Ar)$ are the experimental mass spectroscopic signal intensity, the number of molecules per pulse, and the diffusion coefficient, respectively. To determine the diffusion coefficient of CO_2, the diffusion coefficient of Ar was initially derived through fitting the experimental response of this gas to the Knudsen diffusion model, as described in [45,47]. Eq. (6) was used to obtain the required coefficient:

$$D^{eff}_{Knudsen}(CO_2) = D^{eff}_{Knudsen}(Ar)\sqrt{\frac{M(Ar)}{M(CO_2)}} \tag{6}$$

To obtain the kinetic parameters of CO_2 interaction with spent catalysts, transient responses of CO_2 were fitted to a model considering non-dissociative reversible adsorption of CO_2, as described in Refs. [45, 47]. The TAP reactor was considered as a one pseudo-homogeneous system and divided into three different zones: upstream inert zone, catalyst zone and downstream inert zone. The mass balances for gas-phase and surface species outside the catalyst layer can be described using Eqs. (7) and (8), respectively:

$$\frac{\partial C_i}{\partial t} = D^{eff}_{Knudsen}\frac{\partial^2 C_i}{\partial x^2} \tag{7}$$

$$\theta_i = 0 \tag{8}$$

where C_i – the concentration of CO_2 or Ar, t – the time, and x – the coordinate along the reactor. In the catalyst zone, the reaction term was included in the mass balances for gas-phase (Eq. (9)) and surface species (Eq. (10)):

$$\frac{\partial C_{CO_2}}{\partial t} = D^{eff}_{Knudsen}\frac{\partial^2 C_{CO_2}}{\partial x^2} - N_{total}\cdot(k_+\cdot C_{CO_2}\cdot(1-\theta_{CO_2}) - k_-\cdot\theta_{CO_2}) \tag{9}$$

$$\frac{\partial \theta_{CO_2}}{\partial t} = k_+\cdot C_{CO_2}\cdot(1-\theta_{CO_2}) - k_-\cdot\theta_{CO_2} \tag{10}$$

where N_{total} is the total concentration of surface species and $\theta_{CO_2} = \frac{N_{CO_2}}{N_{total}}$, where N_{CO_2} stands for the concentration of adsorbed CO_2.

The following boundary conditions are applied for solving these partial differential equations:

$$C_i = 0,\ \text{for all species at outlet of the reactor} \tag{11}$$

$$\frac{\partial C_i}{\partial x} = 0,\ t \geq t_{open},\ \text{at the inlet of the reactor} \tag{12}$$

$$\frac{\partial C_{in}}{\partial x} = \left.\frac{\partial C_{in}}{\partial x}\right|_{t=0}\left(1-\frac{t}{t_{open}}\right),\ at\ t < t_{open}, \text{at the inlet of the reactor} \tag{13}$$

where t_{open} – opening time of pulse valve. The condition 12 describes high vacuum conditions at reactor outlet. The second condition (Eq. (13)) considers the fact that the gradient of the gas concentrations at the inlet is zero since the reactor is closed at each time after introduction of the reactant gas. The inlet pulse of reactant is described as gradient for a certain interval, which is dropped linearly up to zero at $t = t_{open}$ (t_{open} is ca. 10 ms) [45].

The resulting system of partial differential equations was solved using a FORTRAN-program applying the numerical routine PDEONE [48]. The search for kinetic parameters was performed in a wide range of possible values (10^{-4}–10^8) using first a genetic algorithm to find good starting values and then the Nelder-Mead simplex algorithms [49]. The quality of fit was characterized by an objective function defined as the sum of squares of the shortest deviation between the respective points of the experimental and simulated data.

2.4. Catalytic tests

Catalytic tests were carried out in an in-house developed setup containing 16-continuous-flow fixed bed stainless-steel tube reactors. The reactors are grouped in sets of 4. Each of these reactor sets has its own heating; the heating design assures high heat-transfer rates between furnace and reactor tube in order to maintain the set temperature even for more exothermic reactions. The outer and inner diameters of reactors are 9.5 and 7.0 mm, respectively. CO_2, H_2, N_2, and He gases were dosed by electronic mass flow controllers (Brooks 5850s). The total flow of feed gases was equally distributed among all the reactors and a bypass channel. The outlet lines from reactors are split at 150 °C into a main flow and a sample portion where the sample portion is connected to a 16-channels automatic valve to select and direct one stream to a gas chromatograph through a heated line (its temperature is 180 °C). A flow of He (3 ml min^{-1} per reactor) is additionally added to this sample stream to prevent condensation of long-chain hydrocarbons. The main flows are led through hot traps where a wax phase is condensed (at 150 °C). The remaining gas streams are combined and passed through a cold trap where H_2O is condensed before they reach the electronic pressure controller (Brooks 5866s).

The catalysts (100 mg, 0.25–0.45 mm) were diluted by SiC (ESK-SiC,

F54, 0.2–0.5 mm fraction) to carry out tests at isothermal condition. The weight fraction of SiC to catalyst was 3:1. Regardless of the mixture of the catalyst and SiC, an additional layer of SiC (800 mg, ESK-SiC, F54, 0.2–0.5 mm fraction) was added on the top to ensure plug flow and to preheat the reaction feed.

The feed components (bypass channel) and the reaction products were analyzed by on-line Agilent 7890A gas chromatograph equipped with a thermal conductivity detector (TCD) and two flame ionization detectors (FID). HP Plot/Q (for CO_2) and MolSieve 5A (for H_2, O_2, N_2, and CO) columns were connected to TCD. For separating hydrocarbons and alcohols, PONA (for C_5-C_{16} hydrocarbons) and HP Plot/Q (for C_1-C_4) columns connected to FIDs were used.

Before catalytic testing the as-prepared catalysts were heated up to 300 °C (the heating rate was 5°/min) in N_2 flow at 1.5 bar (abs.) and after that were reduced in-situ. The hydrogen concentration was increased stepwise, starting with 10 % H_2 in N_2 flow for 10 min, then 30 % H_2 in N_2 flow for 10 min, 50 % H_2 in N_2 flow for 10 min, and finally undiluted CO-H_2 mixture (CO:H_2 was 1:2) for 240 min. During these steps the temperature was kept at 300 °C, pressure at 1.5 bar (abs.) and the residence time was 136 kg s m^{-3}. After the reduction, the catalysts were tested under CO_2-FT conditions (CO_2:H_2:N_2 ratio was 1:3:1) at 15 bar, 300 °C, and at a modified residence time of 328 kg s m^{-3} for 25 h to achieve a steady-state condition. After this, the residence time was varied in a range of 8–328 kg s m^{-3} by adjusting the feed flow rate in a range of 1097–45,000 ml h^{-1}. The time on stream for each condition was 10 h.

The CO_2 conversion (X) and products selectivity were calculated by the following equations:

$$X = 1 - \frac{\dot{n}_{CO_2}^{out}}{\dot{n}_{CO_2}^{in}}, \tag{14}$$

$$S_i = \frac{a_i \cdot \dot{n}_i^{out}}{\sum_{j=1}^{n} a_j \cdot \dot{n}_j^{out}}, \tag{15}$$

where $\dot{n}_{CO_2}^{in}$ – the molar flow of CO_2 in the inlet flow; $\dot{n}_{CO_2}^{out}$ – the molar flow of CO_2 in the outlet flow; S_i – the selectivity of i-product; a_i – the carbon number of i-product; $\dot{n}_i^{out}$ – the molar flow of i-product in the outlet flow. Carbon balance was established to be higher than 98 %.

2.5. The data evaluation

The catalyst activity was determined at different values of the modified residence time τ_{mod} that can be defined as:

$$\tau_{mod} = \frac{m_{cat}}{F}, \tag{16}$$

where m_{cat} – the mass of the catalyst; F – the feed flow. Let M_f be a set of the flows as (F_0, F_1, F_2 … F_n), wherein the set is sorted in ascending order. Thus, F_0 and F_n are 1097 and 45,000 ml h^{-1}, respectively. It can be presented as the set of (F_0, $\gamma_1 F_0$, $\gamma_2 F_0$ … $\gamma_n F_0$), where γ_i – dimensionless constants. Thus, the data with the different modified residence times obtained by varying the feed flow can be presented as data with the fixed flow F_0 and different catalysts mass as (m_{cat}, m_{cat}/γ_1, m_{cat}/γ_2 … m_{cat}/γ_n). In this context, the catalyst bed can be presented as a list of catalyst segments that are graphically shown in Fig. 1.

Where the catalyst mass m_i in segment i can be calculated as:

$$m_i = m_{cat} \Big/ \gamma_{n-i+1} - \sum_{j=1}^{i-1} m_{cat} / \gamma_{n-j+1}, \tag{17}$$

It allows one to calculate the compound formation rates in i-segment according to the following formula:

$$r_j^i = \frac{\dot{n}_j^i - \dot{n}_j^{i-1}}{m_i}, \tag{18}$$

where r_j^i – the rate of the formation of j-compound in the segment i (mol g^{-1} s^{-1}); $\dot{n}_j^i$ and $\dot{n}_j^{i-1}$ – molar flows of j-compound in segments of i and i-1, respectively (mol s^{-1}). The example of the calculation of the segmental rates is presented in the supplementary material (pages 3–4).

The AFS distribution was used for the analysis of the formation rates of hydrocarbons. Let r_n be the formation rate of hydrocarbon with carbon number n. Assuming the absence of the deviations from the ASF distribution, one can show that:

$$\begin{aligned} &\frac{r_n}{r_{n-1}} = \frac{\alpha^{n-1}}{\alpha^{n-2}} \\ &r_n = r_1 \cdot \alpha^{n-1} \\ &\log r_n = n \cdot \log \alpha + \log \frac{r_1}{\alpha} \end{aligned} \tag{19}$$

where α is the chain growth probability. The α and r_1 parameters were calculated by linear fitting in the corresponding coordinates $(n, \log r_n)$ using the data of the hydrocarbon rates calculated by Eq. (18) (see Fig. S1). To calculate the parameters of $\log\alpha$ and $\log r_1$, the rates of C_{3+} hydrocarbons formation were used because it is known that the deviations from the ASF distribution are usually observed for C_1 and C_2 hydrocarbons [33]. The relative 'rates' r^{rel} of hydrocarbons formation were defined as:

$$r_n^{rel} = \frac{r_n^{\exp}}{r_n^{ASF}} \cdot 100\%, \tag{20}$$

where $r_n^{\exp}$ – the formation rate of hydrocarbon with carbon number n calculated by the Eq. (18); r_n^{ASF} – the rate of the formation of hydrocarbon with carbon number n calculated by the equation 19 using α and r_1 parameters. Python programming language (version 3.8.10) [50] and a scientific library NumPy (version 1.20.3) [51] were used for the calculations. Plotly (version 5.1.0) [52] was used to visualize the results.

3. Results and discussion

3.1. Catalyst characterization

Elemental composition and textural characteristics of as-prepared catalysts are summarized in Table S1. The content of dopants in the obtained catalysts measured by ICP corresponds to the theoretical content. It is worth mentioning that the samples are characterized by low values of specific surface area. Wherein, the highest value of 30 m^2 g^{-1} is observed for Fe-K-Al catalyst that was doped by aluminum. Al is known to be a textural promoter that can lead to an increase in surface area [53].

To investigate the reducibility of the obtained catalysts, TPR-H_2 tests were performed. The profiles of TPR-H_2 curves for the as-prepared catalysts are presented in Fig. S3. In the case of the unpromoted Fe

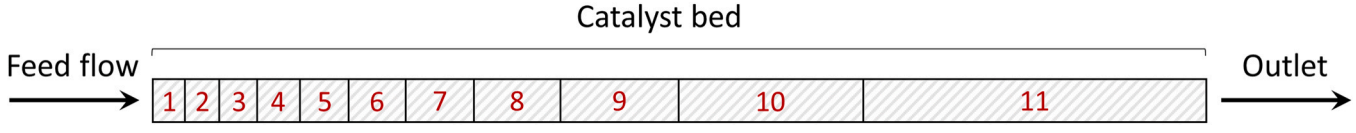

Fig. 1. The derived segments of the catalyst bed.

catalyst, one can see three broad peaks of hydrogen consumption with the maxima at 425, 630, and 780 °C respectively. They relate to three stages process of the reduction of iron oxide ($Fe_2O_3 \rightarrow Fe_3O_4 \rightarrow FeO \rightarrow Fe$) [54]. The profiles of TPR-H_2 curves for the promoted catalysts are similar. However, slight changes in the TPR-H_2 profiles such as shift and broadening of the first peak is observed. The shift of the maximum of the first peak to higher temperature is related to the presence of K, Al and/or Mn in the catalysts as shown in the works [34,53]. Moreover, for the Fe-K-Mn catalyst an additional peak in the temperature range 270–370 °C is observed that may be related to reduction of Mn-containing phases [55].

To identify phase composition of the obtained catalysts, the samples were characterized by XRD. Besides as-prepared catalysts, the catalysts after reduction in CO:H_2 mixture (the ratio was 1:2) (reduced catalysts) and after testing in CO_2 hydrogenation (spent catalysts) were investigated. XRD patterns are presented in Figs. S4-S6. The information about phase composition of the samples are summarized in Table 2. According to the obtained results, the unpromoted Fe catalyst contains only α-Fe_2O_3 hematite phase that is indicated by an existence of corresponding reflexes (PDF 01–087–1164). The phase composition of promoted Fe-K, Fe-K-Al, and Fe-K-Mn catalysts are complex mixtures of different oxides. Besides α-Fe_2O_3 and Fe_3O_4 the K-containing phase $KFe_{11}O_{17}$ was found for all K-doped catalysts. Moreover, the additional phase of Mn_2O_3 was identified in the case of Fe-K-Mn catalyst. No Al-containing phases were detected in the Fe-K-Al catalyst.

After reduction in CO:H_2 mixture, the presence of Fe_5C_2, α-Fe_2O_3, Fe_3O_4 and Fe phases was found for the pure Fe catalyst. Thus, iron carbide was formed after CO:H_2 treatment. The formation of iron carbides from Fe_2O_3 under CO-H_2 mixture is known to proceed via $FeO_x \rightarrow Fe \rightarrow FeC_x$ reactions [56]. It explains the presence of Fe and Fe_3O_4 phases in the reduced catalysts. The iron carbides were also found for reduced Fe-K, Fe-K-Al, and Fe-K-Mn catalysts. Moreover, the reflexes at 10° and 12° at 2θ indicate the presence of n-paraffin in the reduced Fe-K and Fe-K-Mn catalysts. Thus, the formation of hydrocarbons via FT reaction takes place under treatment in CO-H_2 mixture for these catalysts. In the case of the reduced Fe-K-Mn catalyst, Mn was found to be in the form of mixed oxide $Fe_xMn_{1-x}O$ of cubic structure (F*m-3 m* symmetry).

The spent Fe catalyst consists of iron carbides (Fe_5C_2, Fe_7C_3) and Fe_3O_4 phases. The mixture of iron carbides and oxides were also found for the spent K-promoted catalysts. In addition, XRD data indicate the presence of n-paraffin in the Fe-K, Fe-K-Al, Fe-K-Mn catalysts. The phase of $MnCO_3$ was detected for the Fe-K-Mn catalyst. Thus, iron in the spent catalysts is presented in the form of iron carbides and oxides. The content of Fe-containing phases in the spent samples was estimated with the reference intensity ratio (RIR) method. The content of iron carbides are 40, 96, 66, and 93 wt% for the spent Fe, Fe-K, Fe-K-Al, and Fe-K-Mn catalysts, respectively. Thereby, doping by K of Fe-based catalyst stabilizes the formation of iron carbides that is agreed with conclusions made in the works [28]. One can suppose that doping by alumina counteracts the formation of iron carbides under CO/CO_2-H_2 conditions. Al as a textural promoter reduces the formation of carbides from iron oxides during the reduction in CO-H_2. This was also observed in work [57].

Table 2
Phase composition of as-prepared, reduced, and spent catalysts.

Sample	As-prepared	Reduced	Spent
Fe	α-Fe_2O_3	Fe_5C_2, α-Fe_2O_3, Fe_3O_4, Fe	Fe_5C_2 (28)*, Fe_7C_3 (12) Fe_3O_4 (60)
Fe-K	α-Fe_2O_3, Fe_3O_4, $KFe_{11}O_{17}$	Fe_5C_2, Fe_3O_4, n-Paraffin	Fe_5C_2 (96), Fe_3O_4 (4), FeO (<1), n-Paraffin
Fe-K-Al	α-Fe_2O_3, Fe_3O_4, $KFe_{11}O_{17}$	Fe_5C_2, Fe_3O_4, Fe	Fe_5C_2 (48), Fe_7C_3 (18), Fe_3O_4, (34) n-Paraffin
Fe-K-Mn	α-Fe_2O_3, Fe_3O_4, $KFe_{11}O_{17}$, Mn_2O_3	Fe_5C_2, Fe_7C_3, α-Fe_2O_3, Fe_3O_4, $Fe_xMn_{1-x}O$, Fe, n-Paraffin	Fe_5C_2 (93), Fe_3O_4 (7), FeO (<1), $MnCO_3$, n-Paraffin

* Numbers in brackets mean the amount of phase estimated by RIR method (only Fe-containing phases were used for estimation).

3.2. Catalyst activity of the obtained catalysts

To analyze reaction pathways of CO_2 hydrogenation for the obtained samples, catalytic tests were carried out at different CO_2 conversion by varying the total flow rate. Time on stream profiles of CO_2 conversion and product selectivity in CO_2 hydrogenation over the obtained catalysts are presented in Fig. S7. Fig. 2 presents the dependencies of CO, CH_4, alcohols, C_{2+} hydrocarbon selectivity on CO_2 conversion. For all catalysts we observe a decrease in CO selectivity and an increase in hydrocarbon selectivity with rising CO_2 conversion. It is explained by a two-stages mechanism of CO_2-FT where CO is formed as an intermediate compound via RWGS reaction [14,58] that is then subsequently hydrogenated to form hydrocarbons. In the case of unpromoted Fe catalyst, methane selectivity was found to be high reaching 41 % at 30 % CO_2 conversion. The catalysts promoted by K show significant lower values of CH_4 selectivity which are less than 10 % over the whole range of conversion studied which agrees with works [27,59,60]. More detailed information on products distribution and olefins content for the studied catalysts is given in Table S2.

When examining the selectivity-conversion relationships in Fig. 2 closer, different curves are observed for the different catalysts which indicate different kinetics of CO_2/CO hydrogenation over the catalysts. Because values of product selectivity were also obtained at low CO_2 conversion, it allows one to estimate the selectivity of hydrogenation products at zero CO_2 conversion by extrapolation (the calculation procedure can be found in the supplementary material, page 7). In the context of the two-stages mechanism of carbon dioxide hydrogenation where CO is an intermediate compound for hydrocarbons formation, one can expect 100 % of CO selectivity and 0 % of hydrocarbons selectivity at zero CO_2 conversion (see supplementary material, pages 5–6).

In the case of unpromoted Fe catalyst, CO, CH_4 and C_{2+} hydrocarbon selectivity at zero CO_2 conversion were around 76.3 %, 18.5 % and 4.4 % respectively. The high value of methane selectivity indicates a direct route of carbon dioxide hydrogenation to CH_4. This route was discussed in the works [15,35,61] and attributed to the methanation reaction ($CO_2 + 4\ H_2 \rightarrow CH_4 + 2\ H_2O$). It may occur not via FT reaction but as direct hydrogenation on active sites different from the ones responsible for chain growth. Interestingly, a larger-than-zero value of selectivity at zero CO_2 conversion was estimated also for C_{2+} hydrocarbon selectivity. For the unpromoted Fe catalyst it is less clear if a direct route of C_{2+} hydrocarbons formation via FT reaction from CO_2 exists. The non-zero value of C_{2+} selectivity may be related to an error of the data extrapolation due to missing information about selectivity in the range of extremely low CO_2 conversion and a non-linear dependency of C_{2+} selectivity on CO_2 conversion. To check this assumption, Monte Carlo simulations were performed to estimate an error for C_{2+} selectivity at zero conversion for the Fe catalysts (see Fig. S1, the supplementary material). The simulation showed that the value of C_{2+} hydrocarbon selectivity is in a range of 0–10 % which indicates that, based on these data alone, the direct route may not exist and non-zero C_{2+} selectivity at zero conversion could be related to an extrapolation error. A similar selectivity-conversion-dependency was reported for unpromoted Fe_5C_2 catalyst by Junhui Liu et al. [61] where non-zero value of C_{2+} hydrocarbons selectivity at zero CO_2 conversion was claimed but not statistically proven. Nevertheless, they concluded that the direct route of C_{2+} hydrocarbons formation via the FT reaction occurs over this catalyst. However, since the conversion-selectivity curves for the Fe_5C_2 catalyst

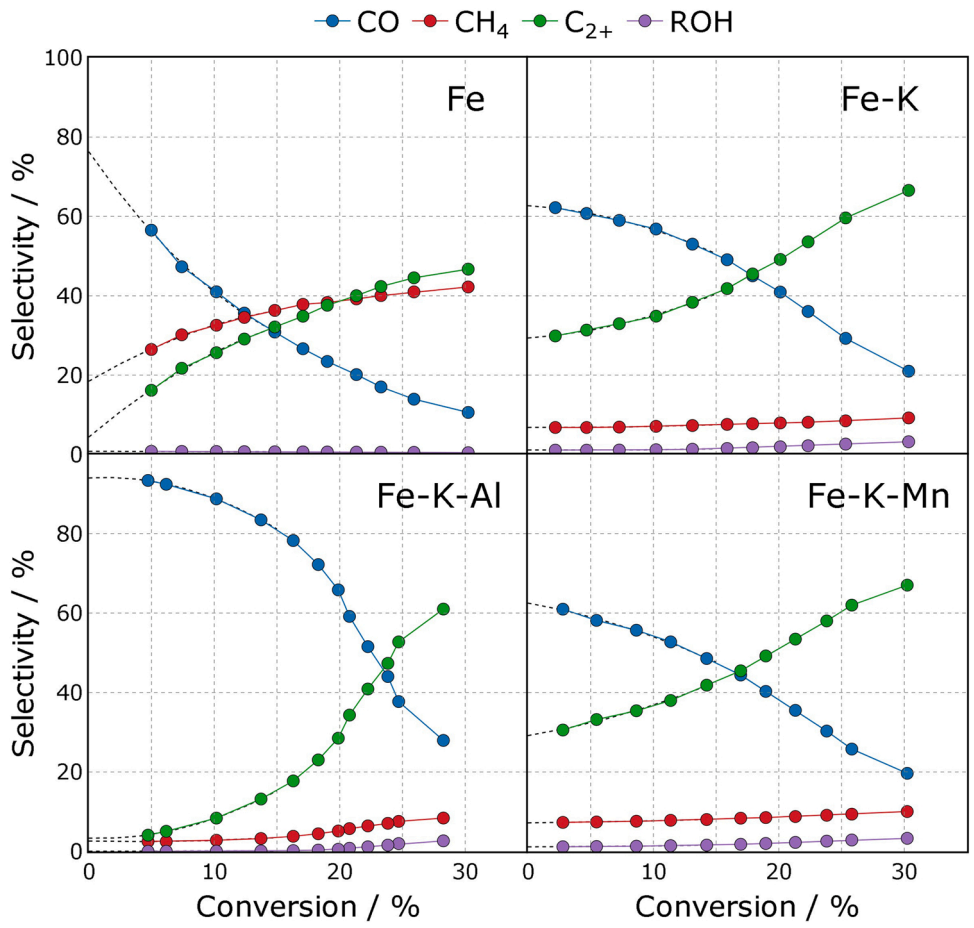

Fig. 2. Selectivity-conversion relationship obtained for different catalysts. Reaction condition: pressure – 15 bar; temperature – 300 °C; CO_2:H_2:N_2 – 1:3:1.

[61] and for the Fe catalyst investigated in the present work are similar and both may be explained by an error of data extrapolation.

For the Fe-K-Al catalyst CO selectivity is around 94 % that is close to 100 % at zero conversion. Wherein the values of methane and C_{2+} hydrocarbons selectivity are less than 4 % and close to zero. The difference form 0 %/100 % is not statistically significantly. Therefore, the data on this catalyst correspond to the conception of two-stage mechanism of CO_2-FT.

For the Fe-K catalyst, the estimated selectivities at zero CO_2 conversion are 62.7 % for CO, 29.4 % for C_{2+} hydrocarbons and 6.8 % for methane. Similar values were obtained for the Fe-K-Mn catalyst (see Table S3, the supplementary material). It is also worth noting that CH_4 selectivity is approximately constant over a wide range of conversion for both Fe-K and Fe-K-Mn catalysts. Non-zero values of CH_4 selectivity at zero CO_2 conversion for these catalysts means that methane is a primary product in CO_2 conversion and, as in the case of the Fe catalyst, the direct formation of methane from CO_2 takes place over these catalysts. Moreover, high values of C_{2+} hydrocarbons selectivity at zero CO_2 conversion are observed for these catalysts. This indicates the presence of direct route of CO_2 hydrogenation to C_{2+} hydrocarbons via FT reaction. It can be explained by a concept that active sites (or ensembles of closely neighbored sites) responsible for chain growth (i.e., hydrocarbon formation via FT) can also activate and hydrogenate CO_2 to CO with hydrogen. Fig. 3 shows different routes of hydrocarbon formation via FT mechanism (excluding the methanation reaction). Direct CO_2-FT means that the active sites responsible for FT reaction are also able to hydrogenate CO_2. Although, active sites for CO and CO_2 hydrogenation to C_{2+} hydrocarbons via FT reaction may also be different leading to a sequential reaction path to hydrocarbons via CO as gas-phase intermediate (see Fig. 3, blue & green route).

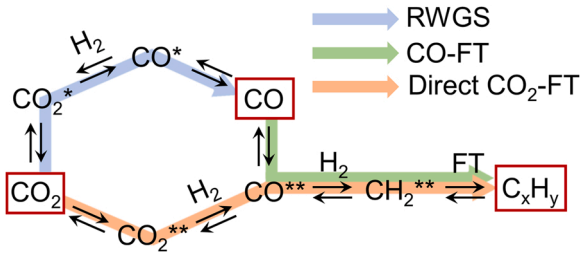

Fig. 3. Different pathways for CO_2/CO hydrogenation via FT. * and ** stand for different surface sites.

Because iron carbides are known to be the active component for CO hydrogenation to form hydrocarbons via FT reaction [7,8], it can be postulated that iron carbides are able to hydrogenate CO_2 to hydrocarbons via FT reaction. In fact, the conversion-selectivity data presented in the Fig. 2 is an experimental proof of the presence of the direct route of CO_2 hydrogenation to C_{2+} hydrocarbons over iron carbides in CO_2-FT. It agrees with the results of first-principles microkinetic modeling performed by Seung Ju Han et al. [62]. They demonstrated that unpromoted iron carbides can catalyze the RWGS reaction. However, it was shown that unpromoted Fe_3O_4 is more active in the RWGS compared to iron carbides.

From the presented results (Fig. 2) one can see that the Fe-K and Fe-K-Mn catalysts show very similar behavior. According to XRD data, the phase composition of both catalysts is similar except for the existence of a Mn-containing phase in the form of $MnCO_3$ in the case of the spent Fe-K-Mn sample. Given the similar performance for Fe-K and Fe-K-Mn, one

can suppose that the Mn in the spent Fe-K-Mn catalyst is preferably in the form of $MnCO_3$ and does not take a part in CO_2 hydrogenation. It is also worth mentioning the difference in activity of the Fe-K and Fe-K-Al catalysts (see Fig. 2) which have complex and differing phase composition according to the XRD data. The fraction of iron oxides in the spent Fe-K-Al catalyst is around 34 wt% and higher than in the spent Fe-K catalyst with just 4 wt%. Thus, the differing amounts of iron oxides may define the difference in the selectivity-conversion relationships of these catalysts.

The analysis of selectivity-conversion relationships allows one to make the following conclusions. The direct CH_4 formation from CO_2 takes place in addition to the RWGS reaction and CO hydrogenation via FT reaction over the Fe, Fe-K, and Fe-K-Mn catalysts. The direct CO_2 hydrogenation to C_{2+} hydrocarbons via FT reaction plays a significant role for at least the Fe-K and Fe-K-Mn catalysts.

3.3. Hydrocarbon distribution analysis

To analyze the hydrocarbon distribution observed over the different catalysts, the ASF distribution was used. Fig. 4 shows the distribution of the hydrocarbons formed in CO_2 hydrogenation over Fe and Fe-K catalysts in corresponding ASF coordinates. The hydrocarbon distribution for Fe-K-Al and Fe-K-Mn catalysts are presented in Fig. S8 (see the supplementary material).

For all catalysts the distributions of the sum of paraffins and olefins corresponds to ASF except for C_1 and C_2 which is typical for products of CO_2 hydrogenation over Fe-based catalysts [33]. The value of the chain growth probability for unpromoted Fe catalyst is around 0.50 and clearly lower than the values for K-doped catalysts which have α in a range 0.65–0.68. The higher chain growth probability for K-doped catalysts correlates with the lower CH_4 selectivity compared to the unpromoted Fe catalyst. Moreover, the low value of α for the Fe catalyst explains why wax was not detected by XRD on the surface of the spent Fe catalyst.

Paraffins and olefins distributions are also presented in Fig. 4 and S7 in the corresponding ASF coordinates. A linear relationship in ASF coordinates is observed in the case of paraffins and olefins distributions for K-promoted catalyst except for ethylene and methane selectivity. Wherein, the values of α for these catalysts is a little higher for paraffins than for olefins (see Fig. 4 and Table S2, the supplementary material). The chain growth probability of the Fe-K catalyst is 0.71 in the case of paraffins distribution compared to α for olefins distribution being 0.66.

For the Fe catalyst, deviation from ASF distribution related to non-linear dependence of hydrocarbon selectivity in the corresponding coordinates is observed for the paraffin distribution. Thus, the chain growth probability depends on the carbon number. In this case, the calculated values of α are 0.18 and 0.68 for carbon number ranges of C_1-C_3 and C_8-C_{10}, respectively.

The reasons of deviations from ASF distribution have been already analyzed and described [63]. An increase in CH_4 selectivity may be related to additional routes of methane formation. One of them is the methanation reaction from CO_2 not via FT reaction [15,35] that agrees with the analysis of conversion-selectivity plots. The other reason may be a double-bond split of α-olefines with higher carbon number leading to additional methane production [21]. Yet another possible explanation was put forward by Wojciechowski and Sarup discussed [64,65] who proposed that the excess of methane selectivity may alternatively be described with a separate parameter of the termination probability. According to their idea, the methane termination probability parameter (the rate constant) is 10 times higher than the one of other hydrocarbons (C_2H_6, C_3H_8 etc.).

The observed decrease in C_2 selectivity compared to the ASF distribution is due to high reactivity of C_2H_4 or surface C_2-intermediates participating in the chain growth compared to olefins with a higher carbon number [66,67]. Our data also confirm that the decrease in C_2 selectivity is only observed in the olefin distribution. The decrease in ethylene selectivity is higher for unpromoted Fe catalyst compared to the catalysts doped by K (see Fig. 4, right) which correlates with the higher activity of unselective hydrogenation to CH_4. It should be also noted that the chain growth probability for the catalysts doped by alkaline metal is higher than for the unpromoted Fe catalyst (see Table S2). It indicates the difference in hydrogenation ability of the obtained catalysts. It is known that unpromoted Fe-based catalysts have higher hydrogenation ability that can be reduced by the promotion of alkali metals leading to enhanced bonding strength of adsorbed CO_2 [18].

The difference in the values of the chain growth probability for olefin and paraffin distributions can be presented as an exponential decrease in olefin-paraffin ratio with the chain length in the form $O_n/P_n \propto \exp(-Cn)$, where $C-$ the natural logarithm of the ratio of α calculated by paraffin and olefin distributions. In the work [63] Van der Laan and Beenackers concluded that the secondary reactions of olefins on Fe-based catalysts are responsible for the observed decrease in olefin-paraffin ratio with increasing carbon number. Wherein, the most

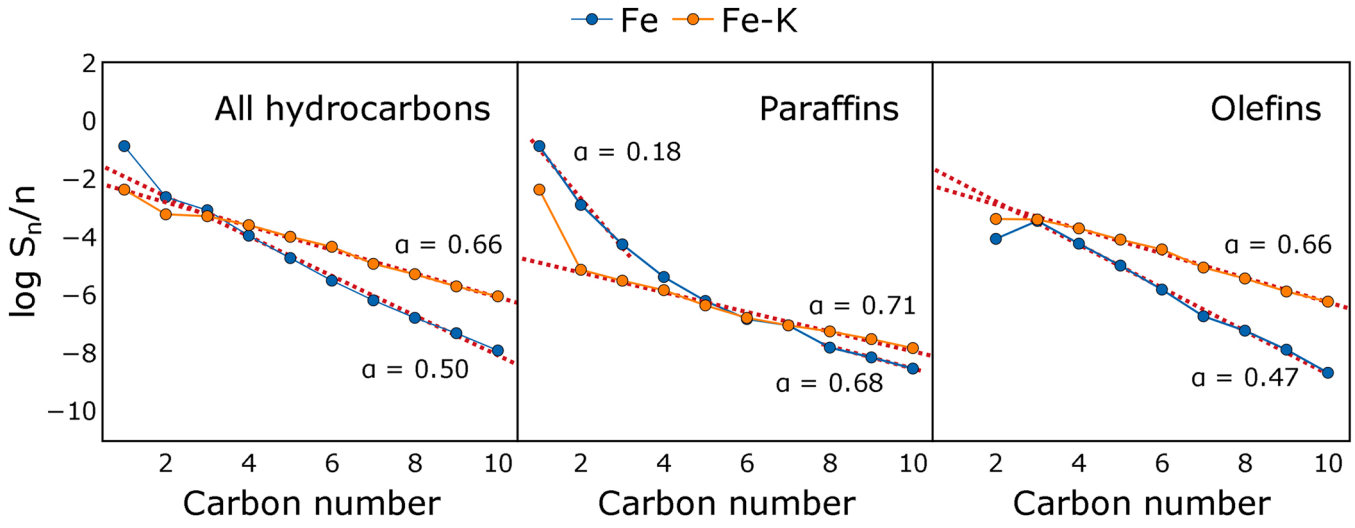

Fig. 4. The hydrocarbons distribution in products of CO_2 hydrogenation over Fe and Fe-K catalysts in ASF coordinates. The C_3-C_{10} range of hydrocarbons was used for fitting the data except for paraffin distribution in the case of Fe catalyst where C_1-C_3 and C_8-C_{10} ranges were used. Reaction condition: pressure – 15 bar; temperature – 300 °C; CO_2:H_2:N_2 – 1:3:1; GHSV – 10,970 ml h^{-1} g^{-1}; time on stream – 25 h.

important secondary reaction is re-adsorption of olefins resulting in initiation of chain growth processes. On the other hand, it may alternatively be explained by the presence of carbon number dependence for olefin desorption. By using an exponential dependence of olefin desorption rate constant, Branislav Todic et al. [68] developed a kinetic model of CO-FT that was able to describe such behavior in olefin and paraffin distributions.

The non-linear relationship of paraffin distribution over carbon number for the Fe catalyst may be related to the presence of two different types of active sites taking part in the molecular processes of the chain growth mechanism as discussed in the work [69]. In this case, the hydrocarbon distribution can be described as:

$$W_n = X{\cdot}n{\cdot}(1-\alpha_1)^2\alpha_1^{n-1} + (1-X){\cdot}n{\cdot}(1-\alpha_2)^2\alpha_2^{n-1}, \quad (21)$$

where X and $1-X$ are the fraction of hydrocarbon products having molecular weight distribution parameters α_1 and α_2 respectively; W_n – weight fraction of an alkane with carbon number n in paraffins. The calculated parameters X, α_1 and α_2 for paraffin distribution in the case of the Fe catalyst are 0.86, 0.15, 0.63 respectively. It implies the presence of 'low-selective' active sites responsible for chain growth via FTS with the chain growth probability of around 0.15. The fraction of hydrocarbons formed by these 'low-selective' sites is predominant and accounts for around 86 % of all hydrocarbons. The existence of the 'low-selective' sites could be one of main the reason for high selectivity of the Fe catalyst to CH_4.

Because catalysts were tested at different CO_2 conversion, we could estimate the chain growth probability α at various CO_2 conversion, see Fig. S9. One can see that the chain growth probability as the key parameter of catalyst selectivity slightly depends on CO_2 conversion which agrees with the data analysis of CO_2 hydrogenation catalysts [33]. However, it is worth mentioning the decrease in α at low CO_2 conversion for the Fe-K-Al catalyst.

3.4. Segmental rates analysis

For a more detailed analysis of the processes occurring in the CO_2 hydrogenation over the obtained catalysts, the segmental rates of CO_2 consumption, CH_4, CO, and C_{2+} formations along the catalyst bed were calculated and are shown in Fig. 5. The overall CO_2 consumption rate decreases along the catalyst bed for all the samples. It is obviously related to a decrease in the concentration of CO_2 and H_2 transforming into products of reactions. Wherein, a sharper decrease in CO_2 consumption is observed for Fe and Fe-K-Al catalysts compared to Fe-K and Fe-K-Mn ones. Already within the front part of the catalyst bed (extending to around 20 % of the bed length for the Fe catalyst and 30 % for Fe-K and Fe-K-Mn catalysts), the rate of CO production decreases to nearly zero where it stays for the remaining part of the bed. A sharper decrease in the CO formation rate is also observed for the initial 20 % bed-part in the case of the Fe-K-Al catalyst. For this catalyst, CO formation rates become negative for the remaining part. It means that the rate of CO-FT becomes higher than the rate of the RWGS reaction.

The rate of methane formation is high at the beginning part and decreases along the catalyst bed for the Fe catalyst. Since CO_2 and H_2 are the main compounds in the gas flow at the beginning of the catalyst bed, carbon dioxide (not carbon monoxide) seems to be responsible for the high rate of CH_4 production at the beginning of the bed. If this catalyst is compared to the ones doped by K, a strong reduction of CH_4 formation is obvious. The initial rate of methane formation for the unpromoted Fe catalyst is around 6 times higher than the rates of the K-doped catalysts.

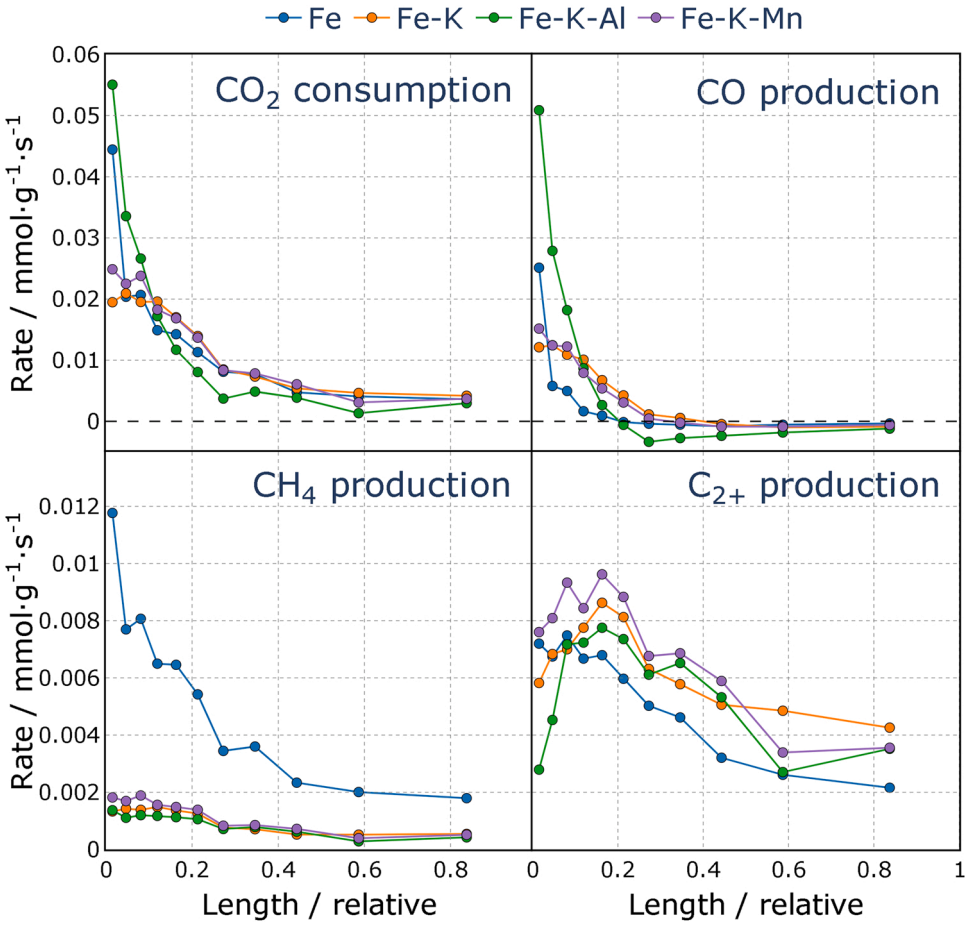

Fig. 5. The segmental rates of CO_2 consumption, CH_4, CO, and C_{2+} formation over the obtained catalysts.

For the rate of formation of C_{2+} hydrocarbons, volcano-like curves are observed along the catalyst bed. However, no maximum is observed in the case of the Fe catalyst. It is worth noting that rates of C_{2+} hydrocarbon production are similar along the catalyst bed for all the catalysts. There is only slightly difference in the front part of the catalyst bed (~ 10 % of length). A slight decrease of C_{2+} hydrocarbon formation rate is seen for the unpromoted Fe catalyst along the whole length. Compared to other catalysts, the Fe-K-Al catalyst is showing a lower C_{2+} formation rate at the initial part of the bed. In conclusion, the rates of hydrocarbon formation over K-doped catalysts do not significantly differ.

The difference in selectivity-conversion relationships (Fig. 2) for the Fe-K-Al catalyst compared to Fe-K and Fe-K-Mn catalysts is rather related to their different activity in the RWGS reaction. As shown above, according to XRD data, the Fe-K-Al catalyst contains 36 wt% iron oxides which is higher than in the Fe-K and Fe-K-Mn catalysts which contain only 4 and 7 wt%, respectively. Since iron oxide is known to be active in the RWGS reaction and to play a key role in CO formation from CO_2 [8], the difference in the content of iron oxide may explain the different activities of the K-promoted catalysts in the RWGS reaction. Indeed, the Fe-K-Al catalyst with the highest iron oxides content was more active in the RWGS reaction than the Fe-K and Fe-K-Mn catalysts. Moreover, the higher amount of iron oxides in the Fe-K-Al catalyst compared to the Fe-K and Fe-K-Mn catalysts could explain the fact that the direct route of CO_2 hydrogenation to C_{2+} hydrocarbons is not observed in the case of the Fe-K-Al catalyst. This may be related to higher activity of iron oxides to catalyze the RWGS reaction compared to direct CO_2-FT route, and, thus, the contribution of the direct route is much lower than the RWGS reaction in CO_2 hydrogenation over the Fe-K-Al catalyst.

The presence of a maximum for hydrocarbon production rate (Figure 5, C_{2+} production) agrees with the concept of the two-stage mechanism of CO_2 hydrogenation where CO is an intermediate compound for hydrocarbons production. In addition, the maximum in the rates of C_{2+} hydrocarbon formation is shifted compared to the maximum of CO concentration (it corresponds to the rate of zero CO production because the rate is the derivative of concentration) along the catalyst bed. This shift might also indicate an additional pathway of hydrocarbon formation from CO_2. On the other hand, it could also be correlated with the increase in H_2O concentration along the bed that may reduce the rate of FT e.g. by competitive adsorption on active sites.

Because the rates of hydrocarbon formation should follow the ASF distribution for an ideal FT, a comparison of the experimental rates and the ones calculated from ASF distribution may give additional information about differences in the mechanism of CO_2 hydrogenation over the 4 catalysts. Fig. 6 presents how the ratio between the observed rates of C_1-C_6 hydrocarbon formation, and the rates predicted via ASF changes along the catalyst bed.

From the presented data one can see that the rates of C_{3+} hydrocarbons formation correspond to the ASF distribution for all the catalysts because of the relative rates being close to one. A slight decrease in the relative rate of C_2 formation with increasing length of the catalyst bed is observed. In the case of CH_4, the formation rates are higher than 1 at the front and decrease along the first part of catalyst bed (around 30 %) and become constant for the rest of the bed (close to 1 for K-promoted catalysts and around 1.5–1.7 for the Fe catalyst). The initial decrease indicates the presence of an additional pathway of methane formation not via FT mechanism which may be the direct methanation reaction discussed above. The rate of CH_4 formation for the unpromoted Fe catalyst decreases also over the first part of the bed, but it remains 1.5–1.7 times

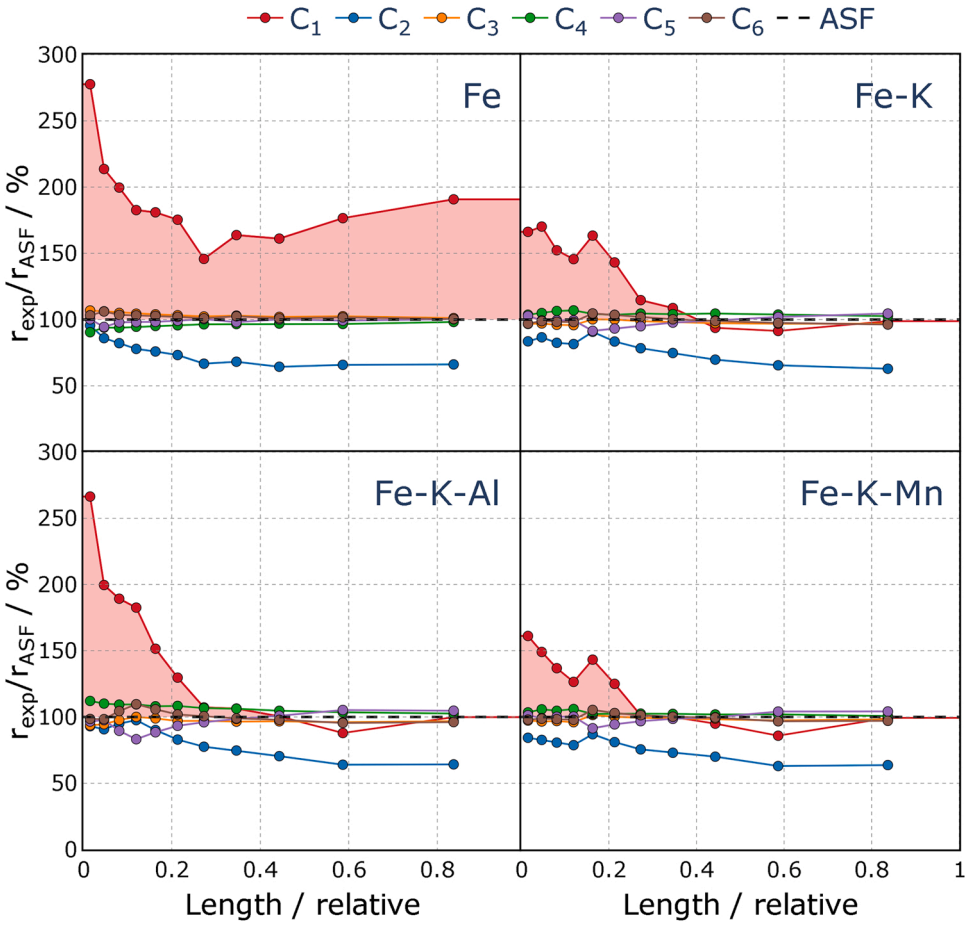

Fig. 6. The relative segmental rates of C_1-C_6 hydrocarbon formation. The "red" shaded region visualizes the excess-methane formation compared to the values calculated by ASF distribution.

higher than the rate calculated by the ASF distribution for the remaining part of the catalyst bed. This deviation from ASF distribution for the remaining part of the bed (>30 % of the bed) could be connected to the existence of low-selective active sites (chain growth probability around 0.18) responsible for hydrocarbons formation only on the Fe catalyst.

3.5. Temporal analysis of CO_2 and H_2 interaction with spent catalysts

The interaction between CO_2 and spent catalysts was studied by pulsing of a CO_2:Ar mixture at 300 °C. A comparison of transient responses of CO_2 and Ar transformed to dimensionless form according to [46] showed that the modified CO_2 response crosses the Ar response (Figs. S10). Such intersection is a fingerprint of reversible adsorption of CO_2 [46]. To derive kinetic parameters of this interaction, the experimental CO_2 responses were fitted to a simple micro-kinetic model, which assumes reversible non-dissociative CO_2 adsorption:

$$\begin{aligned} CO_2 + * &\xrightarrow{k_+} CO_2^* \\ CO_2^* &\xrightarrow{k_-} CO_2 + * \end{aligned} \quad (22)$$

The experimental and simulated responses are compared in Fig. S11. The residual values illustrating the goodness of fit, results of sensitivity and correlation analyses are shown in Table S4 and S5. The values of the parameters resulting from the fitting procedure are summarized in Table 3. Due to a correlation between the total concentration of active sites N_0 and the constant of CO_2 adsorption k_+, only their product $N_0 \cdot k_+ = k_+^{eff}$, further called an effective constant, could be determined. It is worth mentioning that such a correlation is frequently found in kinetic modeling of TAP experiments [70]. For better comparison of the adsorptive properties of spent catalysts the ratio k_+^{eff}/k_- being an efficient equilibrium constant of CO_2 adsorption (K_{eq}^{eff}) is provided in logarithmic form. According to the values in Table 3, doping of Fe with K led to an increase in k_+^{eff} accompanied by the decrease in k_-. Thus, the presence of K increases the equilibrium constant of CO_2 adsorption. The addition of Al led a further increase in this constant. It is worth mentioning that the CO_2 adsorption ability for Fe-K and Fe-K-Mn catalysts are similar in TAP which agrees with the catalytic data where Fe-K and Fe-K-Mn catalysts demonstrated similar activity.

The ability of spent catalysts to activate gas-phase hydrogen was investigated by H/D exchange tests at 300 °C using a H_2:D_2:Ar mixture. Due to negligible amounts of HD formed in these experiments, a quantitative evaluation was not possible. Nevertheless, some relevant information can be obtained from analyzing the shape and the order of appearance of D_2, HD, H_2 and Ar recorded in these experiments (Fig. S12). For the spent Fe and Fe-K-Al catalysts, the HD response is broader than that of D_2 and H_2 and its maximum is situated after those of D_2 and H_2. This is a clear sign of HD formation, i.e., these catalysts are able to break H-H and D-D bonds and to form new H-D bonds. Since the broadening of HD response is more marked over the Fe catalyst, it can be assumed that this catalyst possesses higher activity towards HD formation. No significant difference between the HD and D_2 responses was observed for the Fe-K catalyst versus the Fe-K-Mn one. Both catalysts show lower activity towards HD formation in comparison to the spent Fe and Fe-K-Al catalysts. Therefore, addition of K reduces the ability of Fe-based catalysts to activate gas-phase hydrogen. Using Al as promoter diminishes this effect, whereas the presence of Mn does not have an influence. Considering the phase composition of the spent Fe-K and Fe-K-Mn catalysts, which consist of predominantly iron carbides, and the spent Fe and Fe-K-Al catalysts, which consist of a mixture of iron oxides and carbides phases, one can assume that H_2-D_2 exchange occurs over the surface of iron oxide phase at the condition of TAP experiment.

Table 3
Kinetic parameters of CO_2 adsorption over spent catalysts.

Sample	k_+^{eff}, s^{-1}	k_-, s^{-1}	$\log K_{eq}^{eff}$
Fe	19.4	1.13	2.85
Fe-K	128	0.15	6.75
Fe-K-Al	8190	0.08	11.5
Fe-K-Mn	341	0.28	7.11

3.6. The proposed reaction scheme of CO_2 hydrogenation

Based on the obtained results, we can suggest the reaction pathways occurring at CO_2 hydrogenation over Fe-based catalysts. The scheme of main routes of CO and hydrocarbons formation is presented in Fig. 7.

Besides the previously established routes via RWGS with the formation of CO as intermediate followed by hydrogenation to C_{2+} hydrocarbons via FT reaction, the direct routes of hydrocarbon formation may not be neglected for some catalysts. Methane can be formed as a product of CO_2/CO hydrogenation via FT reaction as well as via an additional direct CO_2 hydrogenation (methanation reaction). The route of direct methanation was shown to occur over all obtained catalysts but to a different extent. The direct route of CO_2 hydrogenation to C_{2+} hydrocarbons via FT reaction plays a role at least for Fe-K and Fe-K-Mn catalysts. The difference in activity of the Fe-K-Al catalyst compared to the Fe-K and Fe-K-Mn catalysts is related to their different ability to catalyze the RWGS reaction. The higher activity of Al-promoted catalyst in RWGS reaction may be explained by the higher content of iron oxide according to XRD data (see Table 2). Thus, in the case of the Fe-K-Al catalyst, the lower contribution (approximately zero) of direct route of CO_2 hydrogenation to C_{2+} hydrocarbons compared to the Fe-K and Fe-K-Mn catalysts may be related to higher activity in RWGS reaction. In the case of the unpromoted Fe catalyst, high CH_4 selectivity compared to K-promoted catalysts was observed that can be caused by the two reasons. The first one is the methanation reaction. The other one is the presence of low-selective active sites with the low chain growth probability (α is around 0.18).

4. Conclusions

The analysis of reaction pathways occurring over Fe-based catalysts demonstrated that except for the RWGS reaction and CO hydrogenation via FT reaction, additional routes of hydrocarbon formation from CO_2 can be important in the carbon dioxide hydrogenation. One of them is the methanation reaction which occurs over all four catalysts. The direct pathway of C_{2+} hydrocarbon formation via FT reaction plays a significant role at least for the Fe-K and Fe-K-Mn catalysts. In the case of the Fe-K catalyst, the spent sample consist of predominantly Fe_5C_2 phase. From this we conclude that certain iron carbides are able to hydrogenate CO_2 directly to C_{2+} hydrocarbons. Accordingly, the concept of requiring iron oxides as an essential active component for catalyzing the RWGS reaction in CO_2-FTS need to be revised.

The ASF analysis of hydrocarbon distribution in the products of CO_2 hydrogenation over the unpromoted Fe catalyst indicates the presence of two types of active sites responsible for hydrocarbon formation via FT reaction. Wherein, low-selective active sites with a chain growth probability of around 0.18 are responsible for high CH_4 selectivity as well as for an additional direct pathway of CO_2 hydrogenation to methane.

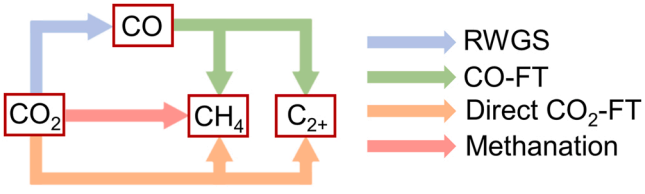

Fig. 7. Scheme including all observed reaction pathways for CO_2 hydrogenation over Fe-based catalysts. The difference between CO-FT and CO_2-FT pathways is presented in Fig. 3.

These sites explain the low selectivity of unpromoted Fe-based catalysts and also the necessity of suppressing their formation by doping with alkaline metals.

The obtained results expand the knowledge about reactions pathway occurring in CO_2 hydrogenation over Fe-based catalysts and are important for accurate kinetic modeling of the process of CO_2-FT synthesis. Moreover, further elucidating the role of iron carbide in the direct pathway of CO_2 hydrogenation to hydrocarbons may help in preparing new catalytic systems with improved performance and high selectivity to the desired products.

Funding

Financial support from Federal Ministry of Education and Research (BMBF) in project InnoSyn (FKZ: 03SF0616B) is gratefully acknowledged. The authors thank Anja Simmula for ICP measurements.

CRediT authorship contribution statement

Aleksandr Fedorov: Conceptualization, Investigation, Methodology, Data curation, Writing – original draft, Writing – review & editing. **Henrik Lund:** Investigation, Writing – review & editing. **Vita A. Kondratenko:** Investigation, Writing – review & editing. **Evgenii V. Kondratenko:** Investigation, Methodology, Writing – review & editing. **David Linke:** Conceptualization, Supervision, Project administration, Funding acquisition, Methodology, Writing – review & editing.

Declaration of Competing Interest

The authors declare that they have no known competing financial interests or personal relationships that could have appeared to influence the work reported in this paper.

Data Availability

The data that has been used is confidential.

Appendix A. Supporting information

Supplementary data associated with this article can be found in the online version at doi:10.1016/j.apcatb.2023.122505.

References

[1] Z.A. Manan, W.N.R. Mohd Nawi, S.R. Wan Alwi, J.J. Klemeš, Advances in process integration research for CO_2 emission reduction – a review, J. Clean. Prod. 167 (2017) 1–13.
[2] F. Marques Mota, D.H. Kim, From CO_2 methanation to ambitious long-chain hydrocarbons: alternative fuels paving the path to sustainability, Chem. Soc. Rev. 48 (2019) 205–259.
[3] W. Wang, S. Wang, X. Ma, J. Gong, Recent advances in catalytic hydrogenation of carbon dioxide, Chem. Soc. Rev. 40 (2011) 3703–3727.
[4] M.D. Garba, M. Usman, S. Khan, F. Shehzad, A. Galadima, M.F. Ehsan, A. S. Ghanem, M. Humayun, CO_2 towards fuels: a review of catalytic conversion of carbon dioxide to hydrocarbons, J. Environ. Chem. Eng. 9 (2021), 104756.
[5] M.V. Landau, N. Meiri, N. Utsis, R. Vidruk Nehemya, M. Herskowitz, Conversion of CO_2, CO, and H_2 in CO_2 hydrogenation to fungible liquid fuels on fe-based catalysts, Ind. Eng. Chem. Res. 56 (2017) 13334–13355.
[6] L. Guo, J. Sun, Q. Ge, N. Tsubaki, Recent advances in direct catalytic hydrogenation of carbon dioxide to valuable C2+ hydrocarbons, J. Mater. Chem. A 6 (2018) 23244–23262.
[7] B. Yao, T. Xiao, O.A. Makgae, X. Jie, S. Gonzalez-Cortes, S. Guan, A.I. Kirkland, J. R. Dilworth, H.A. Al-Megren, S.M. Alshihri, P.J. Dobson, G.P. Owen, J.M. Thomas, P.P. Edwards, Transforming carbon dioxide into jet fuel using an organic combustion-synthesized Fe-Mn-K catalyst, Nat. Commun. 11 (2020) 6395.
[8] J. Wei, Q. Ge, R. Yao, Z. Wen, C. Fang, L. Guo, H. Xu, J. Sun, Directly converting CO_2 into a gasoline fuel, Nat. Commun. 8 (2017) 15174.
[9] G.V. Schulz, Über die Beziehung zwischen Reaktionsgeschwindigkeit und Zusammensetzung des Reaktionsproduktes bei Makropolymerisationsvorgängen, Z. für Phys. Chem. 30B (1935) 379–398.
[10] P.J. Flory, Molecular size distribution in linear condensation polymers1, J. Am. Chem. Soc. 58 (1936) 1877–1885.
[11] R.B. Anderson, R.A. Friedel, H.H. Storch, Fischer-Tropsch reaction mechanism involving stepwise growth of carbon chain, J. Chem. Phys. 19 (1951) 313–319.
[12] G. Henrici-Olivé, S. Olivé, The Fischer-Tropsch synthesis: molecular weight distribution of primary products and reaction mechanism, Angew. Chem. Int. Ed. Engl. 15 (1976) 136–141.
[13] E.S. Lox, G.F. Froment, Kinetics of the Fischer-Tropsch reaction on a precipitated promoted iron catalyst. 2. Kinetic modeling, Ind. Eng. Chem. Res. 32 (1993) 71–82.
[14] T. Riedel, G. Schaub, K.-W. Jun, K.-W. Lee, Kinetics of CO_2 hydrogenation on a K-promoted Fe catalyst, Ind. Eng. Chem. Res. 40 (2001) 1355–1363.
[15] M. Albrecht, U. Rodemerck, M. Schneider, M. Bröring, D. Baabe, E.V. Kondratenko, Unexpectedly efficient CO_2 hydrogenation to higher hydrocarbons over non-doped Fe_2O_3, Appl. Catal. B: Environ. 204 (2017) 119–126.
[16] T. Herranz, S. Rojas, F.J. Pérez-Alonso, M. Ojeda, P. Terreros, J.L.G. Fierro, Hydrogenation of carbon oxides over promoted Fe-Mn catalysts prepared by the microemulsion methodology, Appl. Catal. A: Gen. 311 (2006) 66–75.
[17] B. Liang, T. Sun, J. Ma, H. Duan, L. Li, X. Yang, Y. Zhang, X. Su, Y. Huang, T. Zhang, Mn decorated Na/Fe catalysts for CO_2 hydrogenation to light olefins, Catal. Sci. Technol. 9 (2019) 456–464.
[18] T. Numpilai, N. Chanlek, Y. Poo-Arporn, C.K. Cheng, N. Siri-Nguan, T. Sornchamni, M. Chareonpanich, P. Kongkachuichay, N. Yigit, G. Rupprechter, J. Limtrakul, T. Witoon, Tuning interactions of surface-adsorbed species over Fe−Co/K−Al_2O_3 catalyst by different K contents: selective CO_2 hydrogenation to light olefins, ChemCatChem 12 (2020) 3306–3320.
[19] S.-R. Yan, K.-W. Jun, J.-S. Hong, M.-J. Choi, K.-W. Lee, Promotion effect of Fe–Cu catalyst for the hydrogenation of CO_2 and application to slurry reactor, Appl. Catal. A: Gen. 194–195 (2000) 63–70.
[20] A. Aitbekova, E.D. Goodman, L. Wu, A. Boubnov, A.S. Hoffman, A. Genc, H. Cheng, L. Casalena, S.R. Bare, M. Cargnello, Engineering of ruthenium–iron oxide colloidal heterostructures: improved yields in CO_2 hydrogenation to hydrocarbons, Angew. Chem. Int. Ed. 58 (2019) 17451–17457.
[21] S.-C. Lee, J.-H. Jang, B.-Y. Lee, J.-S. Kim, M. Kang, S.-B. Lee, M.-J. Choi, S.-J. Choung, Promotion of hydrocarbon selectivity in CO_2 hydrogenation by Ru component, J. Mol. Catal. A: Chem. 210 (2004) 131–141.
[22] C. Zhang, C. Cao, Y. Zhang, X. Liu, J. Xu, M. Zhu, W. Tu, Y.-F. Han, Unraveling the role of zinc on bimetallic Fe_5C_2–ZnO catalysts for highly selective carbon dioxide hydrogenation to high carbon α-Olefins, ACS Catal. 11 (2021) 2121–2133.
[23] N. Chaipraditgul, T. Numpilai, C. Kui Cheng, N. Siri-Nguan, T. Sornchamni, C. Wattanakit, J. Limtrakul, T. Witoon, Tuning interaction of surface-adsorbed species over Fe/K-Al_2O_3 modified with transition metals (Cu, Mn, V, Zn or Co) on light olefins production from CO_2 hydrogenation, Fuel 283 (2021), 119248.
[24] T. Witoon, V. Lapkeatseree, T. Numpilai, C. Kui Cheng, J. Limtrakul, CO_2 hydrogenation to light olefins over mixed Fe-Co-K-Al oxides catalysts prepared via precipitation and reduction methods, Chem. Eng. J. 428 (2022), 131389.
[25] B. Liu, S. Geng, J. Zheng, X. Jia, F. Jiang, X. Liu, Unravelling the new roles of Na and Mn promoter in CO_2 hydrogenation over Fe_3O_4-based catalysts for enhanced selectivity to light α-Olefins, ChemCatChem 10 (2018) 4718–4732.
[26] X. Liu, C. Zhang, P. Tian, M. Xu, C. Cao, Z. Yang, M. Zhu, J. Xu, Revealing the effect of sodium on iron-based catalysts for CO_2 hydrogenation: insights from calculation and experiment, J. Phys. Chem. C 125 (2021) 7637–7646.
[27] B. Liang, H. Duan, T. Sun, J. Ma, X. Liu, J. Xu, X. Su, Y. Huang, T. Zhang, Effect of Na promoter on Fe-based catalyst for CO_2 hydrogenation to alkenes, ACS Sustain. Chem. Eng. 7 (2019) 925–932.
[28] N. Fischer, R. Henkel, B. Hettel, M. Iglesias, G. Schaub, M. Claeys, Hydrocarbons via CO_2 hydrogenation over iron catalysts: the effect of potassium on structure and performance, Catal. Lett. 146 (2016) 509–517.
[29] L. Brübach, D. Hodonj, P. Pfeifer, Kinetic analysis of CO_2 hydrogenation to long-chain hydrocarbons on a supported iron catalyst, Ind. Eng. Chem. Res. 61 (2022) 1644–1654.
[30] C. Panzone, R. Philippe, C. Nikitine, L. Vanoye, A. Bengaouer, A. Chappaz, P. Fongarland, Catalytic and kinetic study of the CO_2 hydrogenation reaction over a Fe–K/Al_2O_3 catalyst toward liquid and gaseous hydrocarbon production, Ind. Eng. Chem. Res. 60 (2021) 16635–16652.
[31] S. Saeidi, S. Najari, F. Fazlollahi, M.K. Nikoo, F. Sefidkon, J.J. Klemeš, L.L. Baxter, Mechanisms and kinetics of CO_2 hydrogenation to value-added products: a detailed review on current status and future trends, Renew. Sustain. Energy Rev. 80 (2017) 1292–1311.
[32] C. Panzone, R. Philippe, C. Nikitine, A. Bengaouer, A. Chappaz, P. Fongarland, Development and validation of a detailed microkinetic model for the CO_2 hydrogenation reaction toward hydrocarbons over an Fe–K/Al_2O_3 catalyst, Ind. Eng. Chem. Res. 61 (2022) 4514–4533.
[33] A. Fedorov, D. Linke, Data analysis of CO_2 hydrogenation catalysts for hydrocarbon production, J. CO_2 Util. 61 (2022), 102034.
[34] A.S. Skrypnik, Q. Yang, A.A. Matvienko, V.Y. Bychkov, Y.P. Tulenin, H. Lund, S. A. Petrov, R. Kraehnert, A. Arinchtein, J. Weiss, A. Brueckner, E.V. Kondratenko, Understanding reaction-induced restructuring of well-defined $Fe_xO_yC_z$ compositions and its effect on CO_2 hydrogenation, Appl. Catal. B: Environ. 291 (2021), 120121.
[35] J. Zhu, G. Zhang, W. Li, X. Zhang, F. Ding, C. Song, X. Guo, Deconvolution of the particle size effect on CO_2 hydrogenation over iron-based catalysts, ACS Catal. 10 (2020) 7424–7433.
[36] T. Riedel, M. Claeys, H. Schulz, G. Schaub, S.-S. Nam, K.-W. Jun, M.-J. Choi, G. Kishan, K.-W. Lee, Comparative study of Fischer–Tropsch synthesis with H_2/CO and H_2/CO_2 syngas using Fe- and Co-based catalysts, Appl. Catal. A: Gen. 186 (1999) 201–213.

[37] J. Wang, Z. You, Q. Zhang, W. Deng, Y. Wang, Synthesis of lower olefins by hydrogenation of carbon dioxide over supported iron catalysts, Catal. Today 215 (2013) 186–193.

[38] Z. You, W. Deng, Q. Zhang, Y. Wang, Hydrogenation of carbon dioxide to light olefins over non-supported iron catalyst, Chin. J. Catal. 34 (2013) 956–963.

[39] A. Ramirez, L. Gevers, A. Bavykina, S. Ould-Chikh, J. Gascon, Metal organic framework-derived iron catalysts for the direct hydrogenation of CO_2 to short chain olefins, ACS Catal. 8 (2018) 9174–9182.

[40] Q. Yang, A. Skrypnik, A. Matvienko, H. Lund, M. Holena, E.V. Kondratenko, Revealing property-performance relationships for efficient CO_2 hydrogenation to higher hydrocarbons over Fe-based catalysts: Statistical analysis of literature data and its experimental validation, Appl. Catal. B: Environ. 282 (2021), 119554.

[41] Y. Xu, P. Zhai, Y. Deng, J. Xie, X. Liu, S. Wang, D. Ma, Highly selective olefin production from CO_2 hydrogenation on iron catalysts: a subtle synergy between manganese and sodium additives, Angew. Chem. Int. Ed. 59 (2020) 21736–21744.

[42] C.R. Hubbard, R.L. Snyder, RIR - measurement and use in quantitative XRD, Powder Diffr. 3 (1988) 74–77.

[43] J. Pérez-Ramírez, E.V. Kondratenko, Evolution, achievements, and perspectives of the TAP technique, Catal. Today 121 (2007) 160–169.

[44] K. Morgan, N. Maguire, R. Fushimi, J.T. Gleaves, A. Goguet, M.P. Harold, E. V. Kondratenko, U. Menon, Y. Schuurman, G.S. Yablonsky, Forty years of temporal analysis of products, Catal. Sci. Technol. 7 (2017) 2416–2439.

[45] M. Soick, D. Wolf, M. Baerns, Determination of kinetic parameters for complex heterogeneous catalytic reactions by numerical evaluation of TAP experiments, Chem. Eng. Sci. 55 (2000) 2875–2882.

[46] J.T. Gleaves, G.S. Yablonskii, P. Phanawadee, Y. Schuurman, TAP-2: an interrogative kinetics approach, Appl. Catal. A: Gen. 160 (1997) 55–88.

[47] M. Rothaemel, M. Baerns, Modeling and simulation of transient adsorption and reaction in vacuum using the temporal analysis of products reactor, Ind. Eng. Chem. Res. 35 (1996) 1556–1565.

[48] R.F. Sincovec, N.K. Madsen, Software for nonlinear partial differential equations, ACM Trans. Math. Softw. 1 (1975) 232–260.

[49] F. Gao, L. Han, Implementing the Nelder-Mead simplex algorithm with adaptive parameters, Comput. Optim. Appl. 51 (2012) 259–277.

[50] Python Software Foundation. Python Language Reference, version 3.8. Available at http://www.python.org.

[51] C.R. Harris, K.J. Millman, S.J. van der Walt, R. Gommers, P. Virtanen, D. Cournapeau, E. Wieser, J. Taylor, S. Berg, N.J. Smith, R. Kern, M. Picus, S. Hoyer, M.H. van Kerkwijk, M. Brett, A. Haldane, J.F. del Río, M. Wiebe, P. Peterson, P. Gérard-Marchant, K. Sheppard, T. Reddy, W. Weckesser, H. Abbasi, C. Gohlke, T.E. Oliphant, Array programming with NumPy, Nature 585 (2020) 357–362.

[52] Plotly Technologies Inc, Collaborative data science (2015). https://plotly.com.

[53] O.A. Bulavchenko, A.A. Pochtar', E.Y. Gerasimov, A.V. Fedorov, Y.A. Chesalov, A. A. Saraev, V.A. Yakovlev, V.V. Kaichev, Chemical and texture promoters in Cu-Fe-Al oxide nanocomposite catalysts for combustion of solid fuel gasification products, Appl. Catal. A: Gen. 590 (2020), 117364.

[54] J. Zieliński, I. Zglinicka, L. Znak, Z. Kaszkur, Reduction of Fe_2O_3 with hydrogen, Appl. Catal. A: Gen. 381 (2010) 191–196.

[55] Y. Li, Y. Wan, Y. Li, S. Zhan, Q. Guan, Y. Tian, Low-temperature selective catalytic reduction of NO with NH_3 over Mn_2O_3-doped Fe_2O_3 hexagonal microsheets, ACS Appl. Mater. Interfaces 8 (2016) 5224–5233.

[56] A. Arinchtein, M.-Y. Ye, M. Geske, M. Frisch, R. Kraehnert, Influence of phase composition and pretreatment on the conversion of iron oxides into iron carbides in syngas atmospheres, Catalysts 11 (2021).

[57] M. Xu, X. Liu, G. Song, Y. Cai, B. Shi, Y. Liu, X. Ding, Z. Yang, P. Tian, C. Cao, J. Xu, Regulating iron species compositions by Fe-Al interaction in CO_2 hydrogenation, J. Catal. 413 (2022) 331–341.

[58] R.E. Owen, D. Mattia, P. Plucinski, M.D. Jones, Kinetics of CO_2 hydrogenation to hydrocarbons over iron–silica catalysts, ChemPhysChem 18 (2017) 3211–3218.

[59] A. Russkikh, G. Shterk, B.H. Al-Solami, B.A. Fadhel, A. Ramirez, J. Gascon, Turning waste into value: potassium-promoted red mud as an effective catalyst for the hydrogenation of CO_2, ChemSusChem 13 (2020) 2981–2987.

[60] J. Liu, A. Zhang, X. Jiang, M. Liu, J. Zhu, C. Song, X. Guo, Direct transformation of carbon dioxide to value-added hydrocarbons by physical mixtures of Fe_5C_2 and K-modified Al_2O_3, Ind. Eng. Chem. Res. 57 (2018) 9120–9126.

[61] J. Liu, G. Zhang, X. Jiang, J. Wang, C. Song, X. Guo, Insight into the role of Fe_5C_2 in CO_2 catalytic hydrogenation to hydrocarbons, Catal. Today 371 (2021) 162–170.

[62] S.J. Han, S.-M. Hwang, H.-G. Park, C. Zhang, K.-W. Jun, S.K. Kim, Identification of active sites for CO_2 hydrogenation in Fe catalysts by first-principles microkinetic modelling, J. Mater. Chem. A 8 (2020) 13014–13023.

[63] G.P. Van Der Laan, A.A.C.M. Beenackers, Kinetics and selectivity of the Fischer–Tropsch synthesis: a literature review, Catal. Rev. 41 (1999) 255–318.

[64] B.W. Wojciechowski, The kinetics of the Fischer-Tropsch synthesis, Catal. Rev. 30 (1988) 629–702.

[65] B. Sarup, B.W. Wojciechowski, Studies of the fischer-tropsch synthesis on a cobalt catalyst i. evaluation of product distribution parameters from experimental data, Can. J. Chem. Eng. 66 (1988) 831–842.

[66] C.G. Visconti, M. Martinelli, L. Falbo, A. Infantes-Molina, L. Lietti, P. Forzatti, G. Iaquaniello, E. Palo, B. Picutti, F. Brignoli, CO_2 hydrogenation to lower olefins on a high surface area K-promoted bulk Fe-catalyst, Appl. Catal. B: Environ. 200 (2017) 530–542.

[67] T. Riedel, H. Schulz, G. Schaub, K.-W. Jun, J.-S. Hwang, K.-W. Lee, Fischer–Tropsch on Iron with H_2/CO and H_2/CO_2 as synthesis gases: the episodes of formation of the fischer–tropsch regime and construction of the catalyst, Top. Catal. 26 (2003) 41–54.

[68] B. Todic, T. Bhatelia, G.F. Froment, W. Ma, G. Jacobs, B.H. Davis, D.B. Bukur, Kinetic model of fischer–tropsch synthesis in a slurry reactor on Co–Re/Al_2O_3 catalyst, Ind. Eng. Chem. Res. 52 (2013) 669–679.

[69] L.S. Glebov, G.A. Kliger, The molecular weight distribution of the products of the Fischer-Tropsch synthesis, Russ. Chem. Rev. 63 (1994) 185–195.

[70] Q. Yang, V.A. Kondratenko, S.A. Petrov, D.E. Doronkin, E. Saraçi, H. Lund, A. Arinchtein, R. Kraehnert, A.S. Skrypnik, A.A. Matvienko, E.V. Kondratenko, Identifying Performance Descriptors in CO_2 Hydrogenation over Iron-Based Catalysts Promoted with Alkali Metals, Angew. Chem. Int. Ed. 61 (2022), e202116517.